Effect of Support Redox Character on Catalytic Performance in the Gas Phase Hydrogenation of Benzaldehyde and Nitrobenzene over Supported Gold

Maoshuai Li, Xiaodong Wang, Fernando Cárdenas-Lizana* and Mark A. Keane

Chemical Engineering, School of Engineering and Physical Sciences, Heriot-Watt University, Edinburgh EH14 4AS, Scotland

*corresponding author

Tel: +44(0)131 451 4115, e-mail: f.cardenaslizana @hw.ac.uk

ABSTRACT

A range of oxides (γ-Al_2O_3, TiO_2, ZrO_2, CeO_2, α-Fe_2O_3 and Fe_3O_4) with different redox properties were used to support nano-scale (mean = 2-8 nm) Au and employed in the gas phase hydrogenation of benzaldehyde and nitrobenzene. The catalysts were subjected to TPR, H_2/O_2 titration, H_2 TPD, XRD, TEM/STEM and XPS analysis. The supported Au phase promoted partial reduction of the reducible supports through the action of spillover hydrogen (based on TPD), which generated surface oxygen vacancies (demonstrated by O_2 titration) that inhibit Au particle sintering during catalyst activation. Electron transfer to generate charged Au species (determined by XPS) correlates with support ionisation potential. Higher nitrobenzene hydrogenation (to aniline) *TOF*s were recorded relative to benzaldehyde where rate increased with decreasing Au size (from 8 to 4 nm) with measurably lower *TOF* over Au <3 nm. Strong binding of –CH=O and $–NO_2$ functions to oxygen vacancies resulted in lower hydrogenation rates. Higher temperatures (>413 K) promoted benzaldehyde hydrogenolysis to toluene and benzene. The formation of $Au^{\delta-}$ on non-reducible Al_2O_3 favoured selective reduction of –CH=O with full selectivity to benzyl alcohol at 413 K.

***Keywords*:** Selective hydrogenation; benzaldehyde; nitrobenzene; reducible supports; oxygen vacancies; Au particle size effect.

1. Introduction

The selective hydrogenation of benzaldehyde to benzyl alcohol and nitrobenzene to aniline are important in the production of herbicides, dyes, pigments and fine chemicals [1,2]. Conventional batch synthesis delivers low product yields, is energy inefficient and generates significant waste where exclusive reduction of the carbonyl and nitro group is challenging [3]. Continuous gas phase reaction presents a number of advantages including ease of product/catalyst separation and reduced downtime [4]. Supported Au at the nano-scale (<10 nm) exhibits unique selectivity in the hydrogenation of multi-functional reactants although activity is lower compared with conventional transition metals (Pt, Ru, Pd and Ni) [5] due to the limited capacity of Au to chemisorb/dissociate H_2 [6]. Studies to date on the catalytic hydrogenation of carbonyl (acrolein, benzalacetone, cinnamaldehyde and crotonaldehyde) [7,8] and nitro (chloronitrobenzene, nitrostyrene and nitrobenzaldehyde) [9,10] compounds have shown a dependence on the electronic and geometric properties of the Au phase that are influenced by the support. Smaller Au particles are formed on reducible oxides (***e.g.*** TiO_2 and CeO_2) relative to non-reducible ZrO_2 and SiO_2 [11,12]. Higher turnover frequencies (*TOF*) with decreasing Au size (2-9 nm) has been reported in the hydrogenation of crotonaldehyde [11,13] and nitrobenzene [14] for Au supported on TiO_2, Al_2O_3 and SiO_2. Okumura ***et al***. [11] observed higher alcohol selectivity (from crotonaldehyde) over Au/TiO_2 than Au/Al_2O_3 and Au/SiO_2. Milone and co-workers [15] proposed that reducible iron oxides promote the formation of electron-rich Au through metal-support electron transfer that favours –CH=O reduction. Rojas ***et al.*** [16] concluded that negatively charged Au (on SiO_2) binds the electrophilic carbon in –CH=O facilitating hydrogenation of cinnamaldehyde and benzalacetone.

In nitro group reduction, the high selectivity exhibited by Au/TiO_2 has been attributed to metal-support synergy that promotes $–NO_2$ activation [17]. Shimizu ***et al.*** [18] considered the

role of Al_2O_3 acidity/basicity in tandem with coordinatively unsaturated Au to dissociate H_2 to H^+/H^- at the metal/support interface and selectively reduce $–NO_2$ in the presence of other reactive functionalities. In the hydrogenation of *p*-chloronitrobenzene unwanted hydrodechlorination was reported for $Au/Ce_{0.62}Zr_{0.38}O_2$ and ascribed to C–Cl scission at oxygen vacancy sites [19]. Selective hydrogenation has been well established for Au catalysts but the contribution of the support in modifying Au structure, reactant activation and overall surface reaction mechanism is far from resolved. In this study we compare the catalytic action of Au nanoparticles on oxides (γ-Al_2O_3, ZrO_2, TiO_2, CeO_2, α-Fe_2O_3 and Fe_3O_4) with distinct redox character in the hydrogenation of –CH=O (benzaldehyde) and $–NO_2$ (nitrobenzene) and correlate performance with catalyst structure. We propose surface reaction mechanisms to account for the role of support reducibility in governing –CH=O and $–NO_2$ activation and product selectivity.

2. Experimental

2.1. Catalyst preparation and activation

The supports employed in this study were obtained from commercial sources (γ-Al_2O_3 (Puralox, Condea Vista), TiO_2 (P25, Degussa) and CeO_2 (Grace Davison)) or synthesised (α-Fe_2O_3, Fe_3O_4 and ZrO_2) as described elsewhere [12,20]. Supported Au catalysts were prepared by deposition-precipitation using urea (Riedel-de Haën, 99%) as basification agent. An aqueous solution of urea (100-fold excess) and $HAuCl_4$ (3-7 × 10^{-3} M, 400 cm^3, Sigma Aldrich, 99%) was added to the support (10-30 g). The suspension was stirred and heated (2 K min^{-1}) to 353 K where the pH progressively increased (to 6.5-8.0) as a result of urea decomposition:

$$NH_2\text{-}CO\text{-}NH_2 + 3H_2O \xrightarrow{T=353K} 2NH_4^+ + 2OH^- + CO_2 \quad \textbf{(1)}$$

The solid obtained was separated by filtration, washed with distilled water until Cl free (from $AgNO_3$ test) and dried (2 K min^{-1}) in 45 cm^3 min^{-1} He at 373 K for 5 h. The catalyst

precursors were sieved (ATM fine test sieves) to mean particle diameter = 75 μm and activated at 2 K min^{-1} to 423-673 K in 60 cm^3 min^{-1} H_2. The catalysts were cooled to ambient temperature and passivated in 1% v/v O_2/He for off-line characterisation.

2.2. Catalyst characterisation

Gold content was measured by atomic absorption spectroscopy (Shimadzu AA-6650 spectrometer with an air-acetylene flame) from the diluted extract in aqua regia (25% v/v HNO_3/HCl). The pH associated with the point of zero charge (pH_{pzc}) of the support was determined using the potentiometric mass titration technique described in detail elsewhere [21]. Temperature programmed reduction (TPR), H_2 chemisorption/temperature programmed desorption (TPD), O_2 chemisorption and specific surface area (SSA) measurements were conducted on the CHEM-BET 3000 (Quantachrome) unit equipped with a thermal conductivity detector (TCD) for continuous monitoring of gas composition and the TPR Win™ software for data acquisition/manipulation. Samples were loaded into a U-shaped Pyrex quartz cell (3.76 mm i.d.) and heated in 17 cm^3 min^{-1} (Brooks mass flow controlled) 5% v/v H_2/N_2 at 2 K min^{-1} to 423-673 K for supported Au catalysts and to 1073-1273 K for the supports where the effluent gas passed through a liquid N_2 trap. The activated samples were swept with 65 cm^3 min^{-1} N_2 for 1.5 h, cooled to reaction temperature (413 K) and subjected to a H_2 (BOC, >99.98%) pulse (10 μl) titration procedure. Samples were cooled to ambient temperature, thoroughly flushed in N_2 (65 cm^3 min^{-1}) to remove weakly bound H_2 and subjected to TPD (at 50 K min^{-1}) to 873-1173 K with a final isothermal hold until the signal returned to baseline. Oxygen (BOC, 99.9%) pulse (50 μl) titration at 413 K post-TPR was employed to determine the extent of support reduction where any contribution from Au to total O_2 adsorption is negligible [22]. SSA (reproducible to ±8%) was recorded in 30% v/v N_2/He with undiluted N_2 (BOC, 99.9%) as internal standard. At least three cycles of N_2 adsorption-desorption were employed using the standard single point BET method. Pore

volume was measured using the Micromeritics Gemini VII 2390p system. Prior to analysis, samples were outgassed at 423 K for 1 h in N_2. Total pore volume was obtained at a relative N_2 pressure (P/P_0) = 0.95. X-ray diffractograms (XRD) were recorded on a Bruker/Siemens D500 incident X-ray diffractometer using Cu Kα radiation. Samples were scanned at 0.02º $step^{-1}$ over the range $20º \leq 2\theta \leq 80º$ and the diffractograms identified against the JCPDS-ICDD reference standards, *i.e.* Au (04-0784), γ-Al_2O_3 (10-0425), anatase-TiO_2 (A-TiO_2, 21-1272), rutile-TiO_2 (R-TiO_2, 21-1276), monoclinic-ZrO_2 (M-ZrO_2, 37-1784), tetragonal-ZrO_2 (T-ZrO_2, 50-1089), CeO_2 (43-1002), α-Fe_2O_3 (hematite, 33-0664) and Fe_3O_4 (magnetite, 19-0629). X-ray photoelectron spectroscopic (XPS) analysis was performed on a VG ESCA spectrometer equipped with monochromatised Al Kα radiation (1486 eV). The sample was adhered to conducting carbon tape, mounted in the sample holder and subjected to ultra-high vacuum conditions ($<10^{-8}$ Torr). Full range surveys (Au $4f_{5/2}$ and $4f_{7/2}$ spectra) were collected where the binding energies (BE) were calibrated with respect to the C 1*s* peak (284.5 eV). The Au 4*f* spectra were fitted with abstraction of the Shirley background using the Gaussian-Lorentzian function in XPSPEAK 41. Gold particle morphology (size and shape) was examined by transmission (TEM, JEOL JEM 2011) and scanning transmission (STEM, JEOL 2200FS field emission gun-equipped unit) electron microscopy, employing Gatan Digital Micrograph 1.82 for data acquisition/manipulation. Samples for analysis were dispersed in acetone and deposited on a holey carbon/Cu grid (300 Mesh). The surface area weighted mean Au size (d) was based on a count of at least 300 particles according to

$$d = \frac{\sum_i n_i d_i^3}{\sum_i n_i d_i^2} \qquad \textbf{(2)}$$

where n_i is the number of particles of diameter d_i.

2.3. Catalytic procedure

Catalyst testing was carried out at atmospheric pressure, *in situ* after activation, in a continuous flow fixed bed tubular reactor (i.d. = 15 mm) at 413-573 K under conditions of negligible heat/mass transport limitations. A layer of borosilicate glass beads served as preheating zone, ensuring the organic reactant was vaporised and reached reaction temperature before contacting the catalyst (10-40 mg). Isothermal conditions (±1 K) were maintained by diluting the catalyst bed with ground glass (75 μm). Reaction temperature was continuously monitored by a thermocouple inserted in a thermowell within the catalyst bed. Reactants (benzaldehyde (Fluka, ≥98%), nitrobenzene (Riedel-de Haën, ≥99%) or benzyl alcohol (Riedel-de Haën, ≥99%)) were delivered as an ethanolic (Sigma Aldrich, ≥99%) solution to the reactor *via* a glass/teflon air-tight syringe and teflon line using a microprocessor controlled infusion pump (Model 100 kd Scientific) at a fixed calibrated flow rate. Reactions were conducted in a co-current flow of reactant with H_2 (BOC, >99.98%, 60 cm^3 min^{-1}) at $GHSV = 2 \times 10^4$ h^{-1}. The molar Au to inlet organic molar feed rate (n/F) spanned the range 1.2×10^{-3} - 3.7×10^{-3} h. In blank tests, passage of each reactant in a stream of H_2 through the empty reactor or over the support did not result in any detectable conversion. The reactor effluent was collected in a liquid nitrogen trap for subsequent analysis using a Perkin-Elmer Auto System XL gas chromatograph equipped with a programmed split/splitless injector and a flame ionization detector (FID), employing a DB-1 (50 m × 0.33 mm i.d., 0.20 μm film thickness) capillary column (J&W Scientific). Data acquisition and manipulation were performed using the TurboChrom Workstation Version 6.3.2 (for Windows) chromatography data system. Reactant conversion (X) is defined by

$$X\ (\%) = \frac{[reactant]_{in} - [reactant]_{out}}{[reactant]_{in}} \times 100 \qquad \textbf{(3)}$$

and selectivity (S) to product (j) is given by

$$S_j(\%) = \frac{[product]_{j,\,out}}{[reactant]_{in} - [reactant]_{out}} \times 100 \quad \textbf{(4)}$$

where subscripts "in" and "out" refer to inlet and outlet gas streams. Catalytic activity is also quantified in terms of initial conversion obtained from time on-stream measurements and turnover frequency (*TOF*, rate per active site) calculated using Au dispersion (*D*) obtained from STEM analysis [23] according to:

$$TOF\ (h^{-1}) = \frac{R}{D} \quad \textbf{(5)}$$

where *R* represents reactant consumption rate ($mol_{reactant}\ mol_{metal}^{-1}\ h^{-1}$). Repeated reactions with different samples from the same batch of catalyst delivered raw data reproducibility and mass balances within ±5 %.

3. Results and discussion

3.1. Catalyst characterisation

3.1.1. Structural characteristics and temperature programmed reduction (TPR)

Catalyst physico-chemical characteristics are presented in **Table 1**. SSA range from 11 $m^2\ g^{-1}$ (Au/Fe_3O_4) to 166 $m^2\ g^{-1}$ ($Au/\gamma\text{-}Al_2O_3$) with a corresponding increase in pore volume (0.02-0.36 $cm^3\ g^{-1}$). Values obtained for each catalyst are in good agreement with those reported in the literature [24-27]. The TPR profiles of the supported Au catalyst precursors and corresponding supports are presented in **Fig. 1**. TPR of $Au/\gamma\text{-}Al_2O_3$ **(AI)** and Au/ZrO_2 **(CI)** generated positive signals with associated temperature maxima (T_{max}) at 451 and 476 K, respectively where H_2 consumption matched the requirement for Au^{3+} reduction to Au^0 (**Table 1**). The profiles generated for the $\gamma\text{-}Al_2O_3$ **(AII)** and ZrO_2 **(CII)** supports were featureless with no evidence of H_2 uptake or release, as noted elsewhere [25]. Activation of Au/TiO_2 **(BI)** and Au/CeO_2 **(DI)** presented H_2 consumption peaks at lower temperatures (T_{max} = 364 and 420 K) suggesting weaker metal-support interactions. This is consistent with the work of Delannoy *et al.* [28] who examined the effect of support redox character on Au

reducibility and reported more facile reduction on TiO_2 and CeO_2 relative to Al_2O_3. Hydrogen consumed during TPR of Au/TiO_2 exceeded that required for $Au^{3+} \rightarrow Au^0$ (**Table 1**) and can be attributed to a combined Au reduction with Ti^{4+} conversion to Ti^{3+} at the metal/support interface [29]. The bare TiO_2 support did not exhibit a detectable TPR response **(BII)**. In contrast, thermal treatment of CeO_2 generated two broad signals at 742 K and 1148 K **(DII)** that can be ascribed to surface (523-848 K [30]) and bulk (>1073 K [30]) reduction. Hydrogen consumed during the activation of Au/CeO_2 exceeded Au precursor reduction (**Table 1**) but was significantly lower than the amount needed for full reduction of the CeO_2 carrier (3300 μmol g^{-1}). This suggests partial support reduction where the incorporation of Au on CeO_2 lowered the requisite temperature [31]. TPR of Au/α-Fe_2O_3 **(EI)** resulted in excess H_2 consumption at T_{max} = 389 K whereas TPR of α-Fe_2O_3 **(EII)** generated a signal at 709 K with a broader consumption at T > 800 K suggesting a two-stage reduction of hematite, *i.e.* α-$Fe_2O_3 \rightarrow Fe_3O_4 \rightarrow FeO$. The TPR response for Au/Fe_3O_4 **(FI)** also reveals a down shift in T_{max} relative to the support **(FII)**. The excess H_2 consumed (**Table 1**) fell below that for conversion of Fe_3O_4 to FeO (4250 μmol g^{-1}) again indicative of partial support reduction. Our results demonstrate a more facile reduction of ceria and iron oxide supports due to the presence of Au. Jacobs *et al.* [32] have established partial CeO_2 reduction by spillover hydrogen following dissociative adsorption on supported Au. Furthermore, Scirè and co-workers [33] proposed that Au can weaken the Fe-O bond in iron oxide substrates resulting in greater lattice oxygen mobility and enhanced reducibility.

3.1.2. Hydrogen temperature programmed desorption (TPD) and O_2 chemisorption

Application of TPD to measure surface hydrogen release can allow differentiation between chemisorbed and spillover species which both serve as reactive hydrogen in hydrogenation [34]. The TPD profiles generated for all the catalysts are shown in **Fig. 2**. The literature suggests a lower temperature requirement for H_2 desorption from metal sites (<473

K) compared with release of spillover from the support (>503 K) [35]. A predominant H_2 desorption at $T_{max} \geq 575$ K was observed in this work suggesting that the main contribution is due to spillover. Hydrogen spillover is influenced by the concentration of initiating and acceptor sites, catalyst activation and metal nanoparticle size (*i.e.* degree of contact between participating phases and metal-support interaction(s)) [35]. As a general observation, H_2 release from Au supported on non-reducible (Al_2O_3, ZrO_2) supports (28-51 mmol g_{Au}^{-1}) was significantly greater than that recorded for Au on reducible carriers (≤9 mmol g_{Au}^{-1}). There is compelling evidence in the literature for hydrogen spillover onto Al_2O_3 [34,35] and ZrO_2 [36,37] from supported metals (Pd, Ni, Cu and Ru). The greater H_2 desorption from Au/γ-Al_2O_3 relative to Au/ZrO_2 can be attributed (at least in part) to the higher SSA of Al_2O_3 which can accommodate more spillover. Consumption of spillover hydrogen in the partial reduction of (reducible) titania, ceria and iron oxide can account for the observed lower levels of H_2 TPD [34]. We employed O_2 chemisorption post-TPR as a measure of support reduction [22]. Gold on CeO_2, α-Fe_2O_3 and Fe_3O_4 exhibited greater O_2 uptake (**Table 1**) than that measured for Au/TiO_2, Au/γ-Al_2O_3 and Au/ZrO_2. The difference in O_2 adsorption can be correlated with support redox character [38], where the former group of oxides are characterised by higher redox potentials (E_{redox}) (**Table 1**). Increasing O_2 chemisorption coincided with greater excess H_2 consumption during TPR due to support reduction with the formation of oxygen vacancies. Oxygen deficient sites can be generated by loss of lattice oxygen from reducible metal oxides during thermal treatment in H_2 or CO [39]. Boccuzzi *et al.* [40,41] demonstrated by FTIR spectroscopy the formation of oxygen vacancies following reduction in H_2 of Fe_2O_3, TiO_2 and CeO_2 to 523 K. Moreover, formation of Ce^{3+} defects/surface vacancies in Au/CeO_2-Fe_2O_3 has been linked to the action of spillover hydrogen [42].

3.1.3. X-ray diffraction (XRD) and electron microscopy analysis

Structural analysis by XRD generated the diffractograms presented in **Fig. 3**. There was no clearly discernible peak for Au (at 2θ = 38.1°) which may be due to masking by stronger signals due to the support or the formation of Au particles at the nano-scale and below detection limit (<5 nm) [43]. The XRD pattern of Au/γ-Al_2O_3 is characterised by peaks at 2θ = 37.6°, 39.5°, 45.9° and 67.0° due to cubic γ-Al_2O_3. XRD analysis of Au/TiO_2 revealed a mixture of tetragonal anatase (2θ = 25.3°, 37.8°, 48.1° and 62.8°) and tetragonal rutile (2θ = 27.4°, 36.1°, 41.2°, 54.3°, 56.6°, 69.0° and 69.8°) phases with an anatase:rutile ratio (5:1) that matches the reported Degussa P25 composition [44]. Au/ZrO_2 showed mixed monoclinic (2θ = 28.2°, 31.5°, 34.2°, 34.4°, 35.3°, 40.8°, 49.3°, 50.2°, 50.6° and 55.6°) and tetragonal (2θ = 30.3°, 35.3°, 50.4°, 50.7°, 59.6° and 60.2°) phases with monoclinic/tetragonal ~2. Zirconia phase composition is sensitive to synthesis route and calcination temperature with ratios in the range 1.2-3.2 reported for comparable ZrO_2 preparation and pre-treatment [25]. The XRD patterns of Au on CeO_2, α-Fe_2O_3 and Fe_3O_4 (**Fig. 3(D-F)**) match those of the supports and we can discount bulk support reduction, *i.e.* $CeO_2 \rightarrow Ce_2O_3$, $Fe_2O_3 \rightarrow Fe_3O_4$ and/or $Fe_3O_4 \rightarrow$ FeO.

Gold particle morphology was evaluated by TEM/STEM and the representative images in **Fig. 4** reveal quasi-spherical particles at the nano-scale. Surface area weighted mean Au size was obtained from the size distribution histograms and are recorded in **Table 1**. Gold on γ-Al_2O_3 **(A)** exhibited metal particles in the 1-8 nm range with a mean of 4.3 nm. Appreciably larger Au particles (2-12 nm, mean = 7.0 nm) are observed on ZrO_2 **(C)**, consistent with the report of Mohr *et al*. [45] for Au/ZrO_2 preparation by deposition-precipitation. Reducible CeO_2 **(D)** and α-Fe_2O_3 **(E)** supports show narrower Au size distribution (1-5 nm) and smaller mean values (2.0-2.6 nm) than Au/TiO_2 (**(B)**, 1-9 nm, mean = 4.5 nm). Support oxygen vacancies stabilise transition metal nanoparticles and inhibit sintering [46], which may result

in the formation of smaller Au particles on α-Fe_2O_3 and CeO_2 that bear a greater number of vacancies than Au/TiO_2 (**Table 1**). It should be noted that a wider Au size range and mean (=7.6 nm) characterised Au/Fe_3O_4. Support charge density, reflected in the pH point of zero charge (pH_{pzc}), determines precursor-support interaction in synthesis by deposition-precipitation and can govern ultimate Au size post-TPR. Where solution pH < pH_{pzc}, the support bears a positive charge favouring interaction with anionic Au species. Conversely, where solution pH > pH_{pzc} the Au precursor and support experience repulsive effects due to the negative surface charge resulting in weaker Au-support interaction leading to Au agglomeration during activation [47]. Solution pH controls $AuCl_4^-$ hydrolysis rate *via* substitution of Cl^- by OH^- where $Au(OH)_4^-$ predominates at the final pH (6.5-8.0, see experimental section **2.1.**) [48]. Support pH_{pzc} are given in **Table 1** where the lower value for Fe_3O_4 (5.8) does not favour interaction with (anionic) Au precursor species and can account for larger Au size.

3.1.4. X-ray photoelectron spectroscopy (XPS) analysis

XPS measurements were conducted to probe support effects in modifying Au electronic character. XPS profiles over the Au 4*f* binding energy (BE) region are given in **Fig. 5**. The Au $4f_{7/2}$ BE for Au/γ-Al_2O_3 (83.3 eV) and Au/TiO_2 (83.5 eV) are close to values reported in the literature (Au/Al_2O_3 (83.1 eV) [49] and Au/TiO_2 (83.3 eV) [50]) and fall below the reference metallic Au (83.7-84.0 eV) [51], indicative of electron donation from the support [52]. Gold on CeO_2 (**Table 1**) exhibits an Au $4f_{7/2}$ BE consistent with that published for Au/CeO_2 (84.5 eV) [53] but lower than Au^+ (85.8-86.0 eV) [51]. A partial positive charge ($Au^{\delta+}$) has been proposed for Au/CeO_2 resulting from electron transfer from Au [54]. The data presented in **Fig. 6** show a dependence of Au $4f_{7/2}$ BE on support redox potential where electron transfer from Au is facilitated by carriers with higher potential. Gold electronic structure is also dependent on Au cluster size where any shift in BE is more pronounced with decreasing

coordination number [55]. The formation of smaller particles on Au/CeO_2 can also contribute to an upshift of BE.

3.2. Catalyst activity/selectivity

Benzyl alcohol was the sole product detected in the hydrogenation of benzaldehyde at 413 K. In contrast, gas phase (383-413 K) benzaldehyde conversion over (SiO_2, Al_2O_3, TiO_2, CeO_2 and ZrO_2) supported Cu and Ni resulted in –CH=O hydrogenolysis (to toluene) and/or C–C scission (to benzene) [56,57]. The relationship between benzaldehyde turnover frequency (*TOF* at 413 K) and Au particle size (*d*) is shown in **Fig. 7(I)**. An increase in *TOF* is evident with decreasing Au particle size over the 8-4 nm range which can be linked to greater H_2 uptake under reaction conditions (**Table 1**). The highest specific rate was recorded for $Au/\gamma\text{-}Al_2O_3$ with no detectable activity for catalysts bearing the smallest Au sizes ($Au/\alpha\text{-}Fe_2O_3$ and Au/CeO_2). It has been established that Au exhibits metal to insulator transition for particles ≤3 nm [58] and decreasing hydrogenation activity for smaller Au particles (5→1 nm) has been ascribed to a critical loss of metallic character [59]. Although there is insufficient published data to arrive at any reliable trends regarding Au size effects in –CH=O hydrogenation, we can note the reported decrease in acrolein *TOF* over Au/ZrO_2 for Au particles >4 nm [45] and increase with increasing Au size (1-5 nm) over Au/ZrO_2 and Au/TiO_2 [59]. In contrast to the benzaldehyde reaction, each catalyst was active in nitrobenzene hydrogenation (**Fig. 7(II)**) with a *TOF* maximum for $Au/\gamma\text{-}Al_2O_3$. The greater reactivity of the nitro-reactant agrees with results (for Pt/Al_2O_3) reported by Arai *et al*. [60] where a six-fold higher rate was recorded for nitrobenzene relative to benzaldehyde hydrogenation. This was linked to reaction thermodynamics where nitrobenzene to aniline ($\Delta G_{413\ K}$ = -436 ± 1 kJ mol^{-1}) is more favourable than benzaldehyde hydrogenation to benzyl alcohol ($\Delta G_{413\ K}$ = -24 ± 2 kJ mol^{-1}).

With respect to support reducibility, *TOF* was higher at lower redox potential as shown in **Fig. 8**. Au/ZrO_2 deviates somewhat from the general trend, which we tentatively attribute to the occurrence of larger Au particles (**Fig. 4(C)**) that show low activity in hydrogenation. Lower *TOF* at higher redox potential suggests that oxygen vacancies on reducible supports do not favour –CH=O or $–NO_2$ activation for reaction. It is known that these vacancies can strongly bind adsorbed oxygenated species [61]. Gold on non-reducible γ-Al_2O_3 with the formation of $Au^{\delta-}$ (from XPS analysis) delivered the highest *TOF*. This agrees with published studies [16,62] which have shown that –CH=O activation and alcohol formation is facilitated on negatively charged Au *via* interaction with the electrophilic carbon. Given the negligible benzaldehyde hydrogenation activity over catalysts with smaller (<4 nm) and larger (>7 nm) Au particles at 413 K, we evaluated the effect of reaction temperature on rate and selectivity for Au/CeO_2 and Au/Fe_3O_4 which can be compared with Au/γ-Al_2O_3 in **Table 2**. In each case an increase in *TOF* was observed at higher temperature. A switch was observed from exclusive –CH=O hydrogenation (to benzyl alcohol) at 413 K to hydrogenolysis (to toluene) at 473 K with a predominant aryl-carbonyl hydrogenolytic scission (to benzene) at 573 K over Au/γ-Al_2O_3. A higher temperature (to 498 K) has been shown to promote benzaldehyde conversion to toluene and benzene over Cu/Al_2O_3 [56] and Ni/SiO_2 [63]. Benzaldehyde hydrogenation to benzyl alcohol was not observed over Au/Fe_3O_4 and Au/CeO_2 at any reaction temperature (**Table 2**). Increased temperature generated toluene as principal product with higher selectivity to benzene at 573 K (**Table 2**). Gold on redox supports exhibited a dominant hydrogenolytic character. Reaction of benzyl alcohol as feedstock (at 573 K) over Au/Fe_3O_4 generated toluene as principal product and benzaldehyde (with no detectable benzene) at a similar *TOF* to that recorded for the benzaldehyde reaction (**Table 3**). This points to production of toluene from benzaldehyde *via* consecutive conversion of benzyl alcohol whereas benzene is generated from aldehyde hydrogenolysis. Benzaldehyde was the

principal product in reaction over Au/CeO_2, which can be attributed to oxidative dehydrogenation [64]. This step involves the catalytic action of surface or lattice oxygens associated with the support and the high aldehyde selectivity exhibited by Au/CeO_2 (**Table 3**) must be due to greater oxygen mobility relative to Fe_3O_4 as inferred from O_2 chemisorption (**Table 1**).

Surface oxygen vacancies have been proposed as active sites in a range of applications from automobile exhaust treatment [65], water-gas shift [66] to steam reforming of oxygenates [67]. There is ample evidence that these vacancies can participate in a Mars and van Krevelen (MvK) mechanism with catalyst surface reduction (oxygen depletion) and re-oxidation (oxygen generation) [68]. We propose the involvement of oxygen vacancies in MvK catalytic hydrogenation, as illustrated in **Fig. 9**. The vacancies, created through H_2 chemisorbed on Au that spills onto the support (step A, **Fig. 9(I)**) with H_2O release, act as strong anchoring sites for the carbonyl group (steps B and C) [69], inhibiting reactivity. The stabilised carbonyl function can be activated at elevated temperature (473 K) with benzyl alcohol formation and subsequent hydrogenolysis (step D) or direct hydrogen scission of the –CH=O bond (step E) to benzene. Higher temperature facilitates hydrogen cleavage to give benzene (step F). In contrast, adsorption on non-reducible surfaces (*e.g.* Al_2O_3) *via* the carbonyl function (step A, **Fig. 10**) results in hydrogenation to the alcohol at low reaction temperature (413 K). DFT calculations have shown that a perpendicular adsorption mode is the most stable configuration with –CH=O bonded to the metal oxide surface *via* the oxygen lone electron pair that acts as a Lewis base [70]. FTIR analysis has demonstrated that surface Lewis acid sites on Al_2O_3 promote –CH=O activation in the hydrogenation of nitrobenzaldehyde [71]. Activation and scission of $–CH_2–OH$ (steps B and C, **Fig. 10**), -CH=O (step D) and the aryl-carbonyl bond (steps E and F) is promoted at elevated temperature (473-573 K) with the formation of toluene and benzene. In the conversion of

nitrobenzene (**Fig. 9(II)**) nitro group interaction with oxygen vacancies (steps A and B) has been proposed [72]. Attachment to surface vacancies can also stabilise the nitro group with lower resultant reaction rates but the greater reactivity of the $–NO_2$ function (relative to -CH=O) resulted in measurable activity for each catalyst at 413 K. Interaction of $–NO_2$ with an oxygen vacancy and N–O bond dissociation generates nitrosobenzene (step C) with subsequent reduction to a phenylhydroxylamine intermediate (step D) and aniline formation and release (step E) [68]. Dissociative interaction of H_2O with oxygen vacancies serves to re-oxidise the support.

4. Conclusions

We have demonstrated that oxide support reducibility and Au size (mean = 2-8 nm) governs the catalytic performance of Au in the reduction of –CH=O (benzaldehyde) and $-NO_2$ (nitrobenzene). TPR coupled with oxygen chemisorption has established partial support (TiO_2, CeO_2, α-Fe_2O_3 and Fe_3O_4) reduction due to the action of spillover hydrogen generated by H_2 dissociation on Au. XPS analysis provided evidence of electron transfer between Au and the oxide carriers. Increasing reaction rates were observed with decreasing Au size (from 8 to 4 nm) with measurably lower rates over Au <3 nm. Gold on reducible supports (CeO_2, α-Fe_2O_3 and Fe_3O_4 where $E_{redox} > 0$) exhibited lower benzaldehyde and nitrobenzene *TOF* relative to Au/γ-Al_2O_3, Au/TiO_2 and Au/ZrO_2 ($E_{redox} < 0$), which we attribute to inhibition due to the action of surface oxygen vacancies. There was no measurable benzaldehyde hydrogenation activity over Au/CeO_2, Au/α-Fe_2O_3 and Au/Fe_3O_4 at 413 K. Reaction at higher temperatures generated toluene as principal product with secondary benzene formation and no detectable alcohol production. In contrast, reaction over Au/γ-Al_2O_3 resulted in exclusive benzyl alcohol formation at 413 K with a progressive shift to hydrogenolysis (to toluene and benzene) at higher temperatures.

Acknowledgements

The authors are grateful to Dr. N. Perret for her involvement in this work. EPSRC support for free access to the TEM facility at the University of St. Andrews and financial support to M. Li and X. Wang through the Overseas Research Students Award Scheme (ORSAS) are also acknowledged.

References

[1] M. Turáková, T. Salmi, K. Eränen, J. Wärnå, D. Y. Murzin, M. Králik, Appl. Catal. A: Gen. 499 (2015) 66-76.

[2] J. Scognamiglio, L. Jones, D. Vitale, C. S. Letizia, A. M. Api, Food Chem. Toxicol. 50, Supplement 2 (2012) S140-S160.

[3] V. van Brunt, J. S. Kanel, in: S. Kulprathipanja (Ed.), Reactive Separation Processes, Taylor & Francis, London, 2002, pp. 51-92.

[4] R. J. Giraud, P. A. Williams, A. Sehgal, E. Ponnusamy, A. K. Phillips, J. B. Manley, ACS Sust. Chem. Eng. 2 (2014) 2237-2242.

[5] T. Mitsudome, K. Kaneda, Green Chem. 15 (2013) 2636-2654.

[6] E. Bus, J. T. Miller, J. A. van Bokhoven, J. Phys. Chem. B 109 (2005) 14581-14587.

[7] L. McEwan, M. Julius, S. Roberts, J. C. Q. Fletcher, Gold Bull. 43 (2010) 298-306.

[8] M. Pan, A. J. Brush, Z. D. Pozun, H. C. Ham, W.-Y. Yu, G. Henkelman, G. S. Hwang, C. B. Mullins, Chem. Soc. Rev. 42 (2013) 5002-5013.

[9] A. Corma, P. Serna, H. García, J. Am. Chem. Soc. 129 (2007) 6358-6359.

[10] A. Taketoshi, M. Haruta, Chem. Lett. 43 (2014) 380-387.

[11] M. Okumura, T. Akita, M. Haruta, Catal. Today 74 (2002) 265-269.

[12] X. Wang, N. Perret, M. A. Keane, Appl. Catal. A: Gen. 467 (2013) 575-584.

[13] R. Zanella, C. Louis, S. Giorgio, R. Touroude, J. Catal. 223 (2004) 328-339.

[14] U. Hartfelder, C. Kartusch, M. Makosch, M. Rovezzi, J. Sa, J. A. van Bokhoven, Catal. Sci. Technol. 3 (2013) 454-461.

[15] C. Milone, R. Ingoglia, L. Schipilliti, C. Crisafulli, G. Neri, S. Galvagno, J. Catal. 236 (2005) 80-90.

[16] H. Rojas, G. Díaz, J. J. Martínez, C. Castañeda, A. Gómez-Cortés, J. Arenas-Alatorre, J. Mol. Catal. A: Chem. 363–364 (2012) 122-128.

[17] M. Boronat, P. Concepción, A. Corma, S. González, F. Illas, P. Serna, J. Am. Chem. Soc. 129 (2007) 16230-16237.

[18] K. Shimizu, Y. Miyamoto, T. Kawasaki, T. Tanji, Y. Tai, A. Satsuma, J. Phys. Chem. C 113 (2009) 17803-17810.

[19] X. Wang, N. Perret, J. J. Delgado, G. Blanco, X. Chen, C. M. Olmos, S. Bernal, M. A. Keane, J. Phys. Chem. C 117 (2013) 994-1005.

[20] F. Cárdenas-Lizana, S. Gómez-Quero, L. Kiwi-Minsker, M. A. Keane, Int. J. Nanotech. 9 (2012) 92-112.

[21] N. Perret, F. Cárdenas-Lizana, D. Lamey, V. Laporte, L. Kiwi-Minsker, M. A. Keane, Top. Catal. 55 (2012) 955-968.

[22] G. C. Bond, Molecules 17 (2012) 1716-1743.

[23] M. Li, X. Wang, N. Perret, M. A. Keane, Catal. Commun. 46 (2014) 187-191.

[24] J. Lenz, B. C. Campo, M. Alvarez, M. A. Volpe, J. Catal. 267 (2009) 50-56.

[25] X. Zhang, H. Shi, B.-Q. Xu, J. Catal. 279 (2011) 75-87.

[26] G. Jacobs, T. K. Das, Y. Zhang, J. Li, G. Racoillet, B. H. Davis, Appl. Catal. A: Gen. 233 (2002) 263-281.

[27] B. Campo, C. Petit, M. A. Volpe, J. Catal. 254 (2008) 71-78.

[28] L. Delannoy, N. Weiher, N. Tsapatsaris, A. M. Beesley, L. Nchari, S. L.M. Schroeder, C. Louis, Top. Catal. 44 (2007) 263-273.

[29] M. Ousmane, L. F. Liotta, D. di Carlo, G. Pantaleo, A. M. Venezia, G. Deganello, L. Retailleau, A. Boreave, A. Giroir-Fendler, Appl. Catal. B: Environ. 101 (2011) 629-637.

[30] F. Arena, P. Famulari, G. Trunfio, G. Bonura, F. Frusteri, L. Spadaro, Appl. Catal. B: Environ. 66 (2006) 81-91.

[31] D. Andreeva, V. Idakiev, T. Tabakova, L. Ilievaa, P. Falaras, A. Bourlinos, A. Travlos, Catal. Today 72 (2002) 51-57.

[32] G. Jacobs, S. Ricote, P. M. Patterson, U. M. Graham, A. Dozier, S. Khalid, E. Rhodus, B. H. Davis, Appl. Catal. A: Gen. 292 (2005) 229-243.

[33] S. Scirè, C. Crisafulli, S. Minicò, G. G. Condorelli, A. Di Mauro, J. Mol. Catal. A: Chem. 284 (2008) 24-32.

[34] R. Prins, Chem. Rev. 112 (2012) 2714-2738.

[35] C. Amorim, M. A. Keane, J. Hazard. Mater. 211–212 (2012) 208-217.

[36] K.-D. Jung, A. T. Bell, J. Catal. 193 (2000) 207-223.

[37] H. Ishikawa, J. N. Kondo, K. Domen, J. Phys. Chem. B 103 (1999) 3229-3234.

[38] D. Haffad, U. Kameswari, M. M. Bettahar, A. Chambellan, J. C. Lavalley, J. Catal. 172 (1997) 85-92.

[39] M. V. Ganduglia-Pirovano, A. Hofmann, J. Sauer, Surf. Sci. Rep. 62 (2007) 219-270.

[40] F. Boccuzzi, A. Chiorino, M. Manzoli, D. Andreeva, T. Tabakova, J. Catal. 188 (1999) 176-185.

[41] T. Tabakova, F. Boccuzzi, M. Manzoli, D. Andreeva, Appl. Catal. A: Gen. 252 (2003) 385-397.

[42] T. Tabakova, G. Avgouropoulos, J. Papavasiliou, M. Manzoli, F. Boccuzzi, K. Tenchev, F. Vindigni, T. Ioannides, Appl. Catal. B: Environ. 101 (2011) 256-265.

[43] G. C. Bond, C. Louis, D. T. Thompson, Catalysis by Gold, Imperial College Press, London,

2006.

[44] G. L. Haller, D. E. Resasco, Adv. Catal. 36 (1989) 173-235.

[45] C. Mohr, H. Hofmeister, P. Claus, J. Catal. 213 (2003) 86-94.

[46] L. F. Liotta, G. Pantaleo, F. Puleo, A. M. Venezia, Catal. Today 187 (2012) 10-19.

[47] N. Perret, X. Wang, L. Delannoy, C. Potvin, C. Louis, M. A. Keane, J. Catal. 286 (2012) 172-183.

[48] F. Moreau, G. C. Bond, A. O. Taylor, J. Catal. 231 (2005) 105-114.

[49] S. Arrii, F. Morfin, A. J. Renouprez, J. L. Rousset, J. Am. Chem. Soc. 126 (2004) 1199-1205.

[50] S. Schimpf, M. Lucas, C. Mohr, U. Rodemerck, A. Brückner, J. Radnick, H. Hofmeister, P. Claus, Catal. Today 72 (2002) 63-78.

[51] A. M. Visco, F. Neri, G. Neri, A. Donato, C. Milone, S. Galvagno, Phys. Chem. Chem. Phys. 1 (1999) 2869-2873.

[52] Y.-F. Han, Z. Zhong, K. Ramesh, F. Chen, L. Chen, T. White, Q. Tay, S. N. Yaakub, Z. Wang, J. Phys. Chem. C 111 (2007) 8410-8413.

[53] W. Deng, A. I. Frenkel, R. Si, M. Flytzani-Stephanopoulos, J. Phys. Chem. C 112 (2008) 12834-12840.

[54] A. N. Pestryakov, V. V. Lunin, A. N. Kharlanov, D. I. Kochubey, N. Bogdanchikova, A. Yu. Stakheev, J. Mol. Struct. 642 (2002) 129-136.

[55] S. Peters, S. Peredkov, M. Neeb, W. Eberhardt, M. Al-Hada, Surf. Sci. 608 (2013) 129-134.

[56] A. Saadi, Z. Rassoul, M. M. Bettahar, J. Mol. Catal. A: Chem. 164 (2000) 205-216.

[57] A. Saadi, R. Merabti, Z. Rassoul, M. M. Bettahar, J. Mol. Catal. A: Chem. 253 (2006) 79-85.

[58] M. Chen, D. W. Goodman, Acc. Chem. Res. 39 (2006) 739-746.

[59] P. Claus, A. Brückner, C. Mohr, H. Hofmeister, J. Am. Chem. Soc. 122 (2000) 11430-11439.

[60] M. Arai, A. Obata, Y. Nishiyama, React. Kinet. Catal. Lett. 61 (1997) 275-280.

[61] C. T. Campbell, C. H. F. Peden, Science 309 (2005) 713-714.

[62] C. Milone, C. Crisafulli, R. Ingoglia, L. Schipilliti, S. Galvagno, Catal. Today 122 (2007) 341-351.

[63] M. A. Keane, J. Mol. Catal. A: Chem. 118 (1997) 261-269.

[64] M. A. Vannice, D. Poondi, J. Catal. 169 (1997) 166-175.

[65] H. He, H. X. Dai, L. H. Ng, K. W. Wong, C. T. Au, J. Catal. 206 (2002) 1-13.

[66] J. A. Rodriguez, S. Ma, P. Liu, J. Hrbek, J. Evans, M. Pérez, Science 318 (2007) 1757-1760.

[67] T.-J. Huang, H.-J. Lin, T.-C. Yu, Catal. Lett. 105 (2005) 239-247.

[68] C. Doornkamp, V. Ponec, J. Mol. Catal. A: Chem. 162 (2000) 19-32.

[69] A. Sepúlveda-Escribano, F. Coloma, F. Rodríguez-Reinoso, J. Catal. 178 (1998) 649-657.

[70] S. Sitthisa, T. Sooknoi, Y. Ma, P. B. Balbuena, D. E. Resasco, J. Catal. 277 (2011) 1-13.

[71] N. Perret, X. Wang, T. Onfroy, C. Calers, M. A. Keane, J. Catal. 309 (2014) 333-342.

[72] A. Maltha, S. C. van Wermeskerken, T. L. F. Favre, P. Angevaare, E. J. Grootendorst, C. A.

Koutstaal, A. P. Zuur, V. Ponec, Catal. Today 10 (1991) 387-391.

Table 1: Gold loading, specific surface area (SSA), pore volume, Au particle size from TEM/STEM analysis (d), H_2 consumption during temperature programmed reduction (TPR) and requirements for reduction of the Au precursor, H_2 and O_2 chemisorption (post-TPR), H_2 released during temperature programmed desorption (TPD), support point of zero charge (pH_{pzc}), Au $4f_{7/2}$ binding energy (BE) and standard redox potential (E_{redox}) of the supports.

Catalyst	Au loading (% w/w)	SSA ($m^2\ g^{-1}$)	Pore volume ($cm^3\ g^{-1}$)	d (nm)	TPR H_2 consumption ($\mu mol\ g^{-1}$)	H_2 chemisorption ($\mu mol\ g_{Au}^{-1}$)	H_2 desorbed ($mmol\ g_{Au}^{-1}$)	O_2 chemisorption ($\mu mol\ g^{-1}$)	pH_{pzc}	Au $4f_{7/2}$ BE (eV)	E_{redox} (V)
$Au/\gamma\text{-}Al_2O_3$	1.1	166	0.36	4.3	87[a]/84[b]	318	51	1	7.1	83.3	-1.7
Au/TiO_2	1.3	44	0.12	4.5	126[a]/91[b]	162	9	5	6.7	83.5	-0.6
Au/ZrO_2	1.0	93	0.13	7.0	56[a]/61[b]	137	28	3	7.4	83.6	-1.5
Au/CeO_2	3.0	108	0.15	2.0	553[a]/231[b]	58	6	132	6.8	84.7	1.6
$Au/\alpha\text{-}Fe_2O_3$	1.2	57	0.16	2.6	750[a]/93[b]	72	4	168	8.1	84.2	0.8
Au/Fe_3O_4	0.9	11	0.02	7.6	500[a]/90[b]	<1	<1	58	5.8	84.1	0.1

[a]experimental value obtained from TPR analysis
[b]calculated value for $Au^{3+} \rightarrow Au^0$

Table 2: Effect of reaction temperature on turnover frequency (*TOF*) and product selectivity (S_j) for the conversion of benzaldehyde over Au/γ-Al_2O_3, Au/Fe_3O_4 and Au/CeO_2.

Catalyst	*T* (K)	*TOF* (h^{-1})	$S_{benzene}$ (%)	$S_{toluene}$ (%)	$S_{benzyl\ alcohol}$ (%)
Au/γ-Al_2O_3	413	82	0	0	100
	473	126	0	70	30
	573	258	71	21	8
Au/Fe_3O_4	413	[a]	-	-	-
	473	192	10	90	0
	573	378	21	79	0
Au/CeO_2	413	[a]	-	-	-
	473	8	0	100	0
	573	49	20	80	0

[a]no detectable activity

Table 3: Benzyl alcohol turnover frequency (*TOF*) and product selectivity (S_j) for reaction over Au/Fe_3O_4 and Au/CeO_2: T = 573 K.

Catalyst	*TOF* (h^{-1})	$S_{benzene}$ (%)	$S_{toluene}$ (%)	$S_{benzaldehyde}$ (%)
Au/Fe_3O_4	364	0	95	5
Au/CeO_2	17	8	17	75

Figure captions

Fig.1: Temperature programmed reduction (TPR) profiles for **(I)** supported Au (solid lines) and **(II)** the corresponding supports (dotted lines): **(A)** γ-Al_2O_3, **(B)** TiO_2, **(C)** ZrO_2, **(D)** CeO_2, **(E)** α-Fe_2O_3, **(F)** Fe_3O_4.

Fig. 2: Hydrogen temperature programmed desorption (TPD) profiles: **(A)** Au/γ-Al_2O_3, **(B)** Au/TiO_2, **(C)** Au/ZrO_2, **(D)** Au/CeO_2, **(E)** Au/α-Fe_2O_3, **(F)** Au/Fe_3O_4.

Fig. 3: XRD patterns for activated/passivated **(A)** Au/γ-Al_2O_3, **(B)** Au/TiO_2, **(C)** Au/ZrO_2, **(D)** Au/CeO_2, **(E)** Au/α-Fe_2O_3 and **(F)** Au/Fe_3O_4; reference JCPDS-ICDD patterns (see card No. in **section 2.2**) are included for Au, γ-Al_2O_3, anatase TiO_2 (A-TiO_2), rutile TiO_2 (R-TiO_2), monoclinic ZrO_2 (M-ZrO_2), tetragonal ZrO_2 (T-ZrO_2), CeO_2, α-Fe_2O_3 (hematite) and Fe_3O_4 (magnetite).

Fig. 4: Representative TEM/STEM images of **(A)** Au/γ-Al_2O_3, **(B)** Au/TiO_2, **(C)** Au/ZrO_2, **(D)** Au/CeO_2, **(E)** Au/α-Fe_2O_3 and **(F)** Au/Fe_3O_4 with associated Au size distribution histograms.

Fig. 5: XPS spectra over the Au 4*f* region for **(A)** Au/γ-Al_2O_3, **(B)** Au/TiO_2, **(C)** Au/ZrO_2, **(D)** Au/CeO_2, **(E)** Au/α-Fe_2O_3 and **(F)** Au/Fe_3O_4; experimental data are given by ■ where lines represent data fitting with peak deconvolution.

Fig. 6: Dependence of Au $4f_{7/2}$ binding energy (BE) on the standard redox potential (E_{redox}) of the oxide supports: **(A)** ◆ Au/γ-Al_2O_3; **(B)** ◄ Au/TiO_2; **(C)** ► Au/ZrO_2; **(D)** ▲ Au/CeO_2; **(E)** ▼ Au/α-Fe_2O_3; **(F)** ■ Au/Fe_3O_4.

Fig. 7: (I) Benzaldehyde (T = 413 K, n/F = 1.2 × 10^{-3} h) and **(II)** nitrobenzene (T = 413 K, n/F = 3.7 × 10^{-3} h) turnover frequency (*TOF*) as a function of Au particle size (d): **(A)** ◆ Au/γ-Al_2O_3; **(B)** ◄ Au/TiO_2; **(C)** ► Au/ZrO_2; **(D)** ▲ Au/CeO_2; **(E)** ▼ Au/α-Fe_2O_3; **(F)** ■ Au/Fe_3O_4.

Fig. 8: Dependence of turnover frequency (*TOF*) on the standard redox potential of the oxide supports (E_{redox} from [38]) in **(I)** benzaldehyde and **(II)** nitrobenzene hydrogenation: **(A)** ◆ Au/γ-Al_2O_3; **(B)** ◄ Au/TiO_2; **(C)** ► Au/ZrO_2; **(D)** ▲ Au/CeO_2; **(E)** ▼ Au/α-Fe_2O_3; **(F)** ■ Au/Fe_3O_4.

Fig. 9: Proposed reaction mechanism for **(I)** benzaldehyde and **(II)** nitrobenzene hydrogenation over Au on reducible supports; M = Ce or Fe.

Fig. 10: Proposed reaction mechanism for benzaldehyde hydrogenation over Au/γ-Al_2O_3 (M = Al) at different reaction temperatures.

Fig. 1

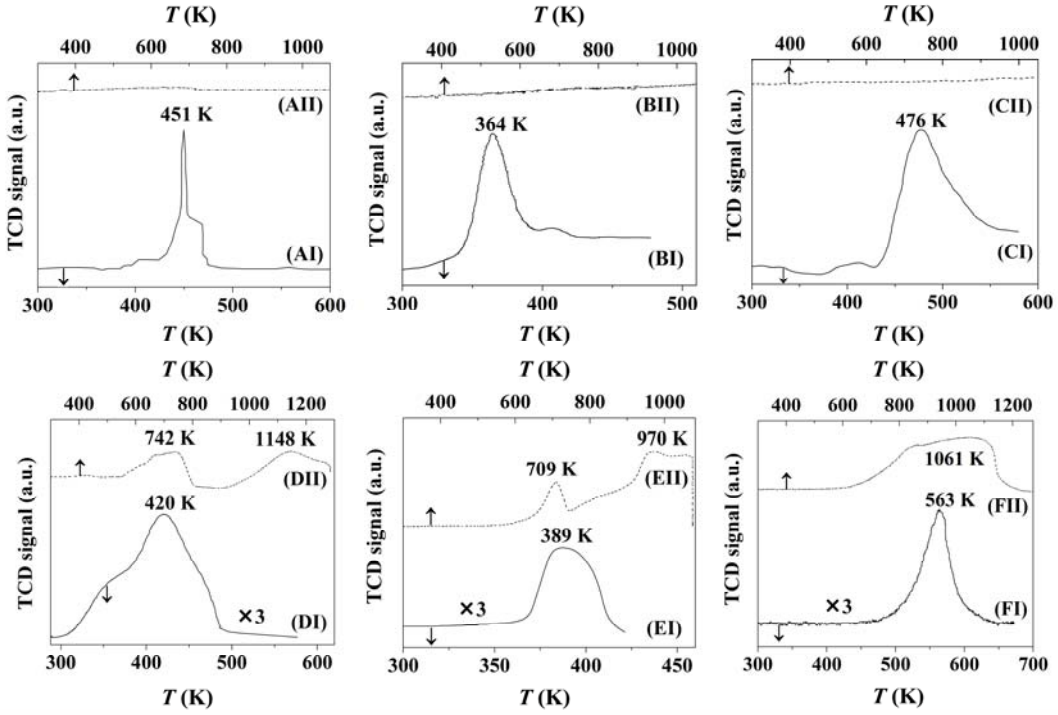
T (K)
TCD signal (a.u.)
451 K
(AII)
(AI)
364 K
(BII)
(BI)
476 K
(CII)
(CI)
742 K
1148 K
(DII)
420 K
×3
(DI)
970 K
709 K
(EII)
389 K
×3
(EI)
1061 K
563 K
(FII)
×3
(FI)

Fig. 2

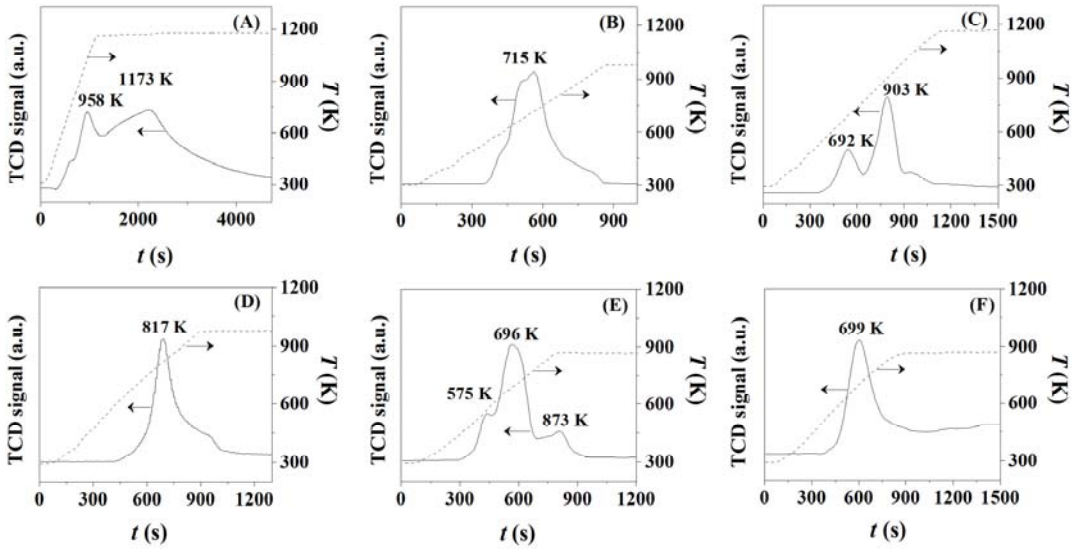
(A)
1173 K
958 K
(B)
715 K
(C)
903 K
692 K
(D)
817 K
(E)
696 K
575 K
873 K
(F)
699 K
TCD signal (a.u.)
T (K)
t (s)

Fig. 3

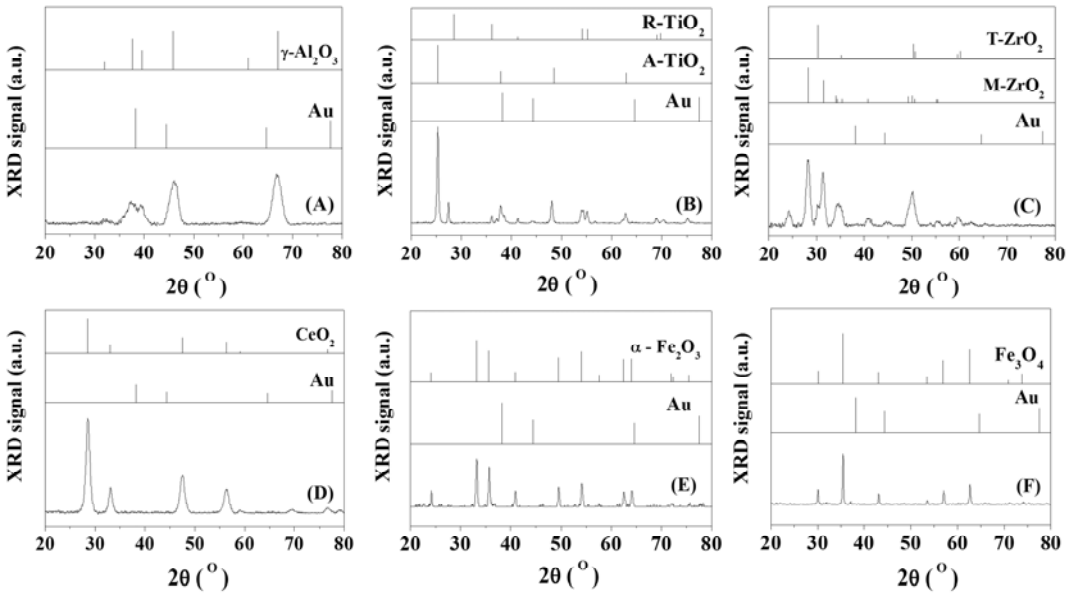
XRD signal (a.u.)
γ-Al2O3
Au
(A)
R-TiO2
A-TiO2
Au
(B)
T-ZrO2
M-ZrO2
Au
(C)
CeO2
Au
(D)
α - Fe2O3
Au
(E)
Fe3O4
Au
(F)
20 30 40 50 60 70 80
2θ (O)

Fig. 4

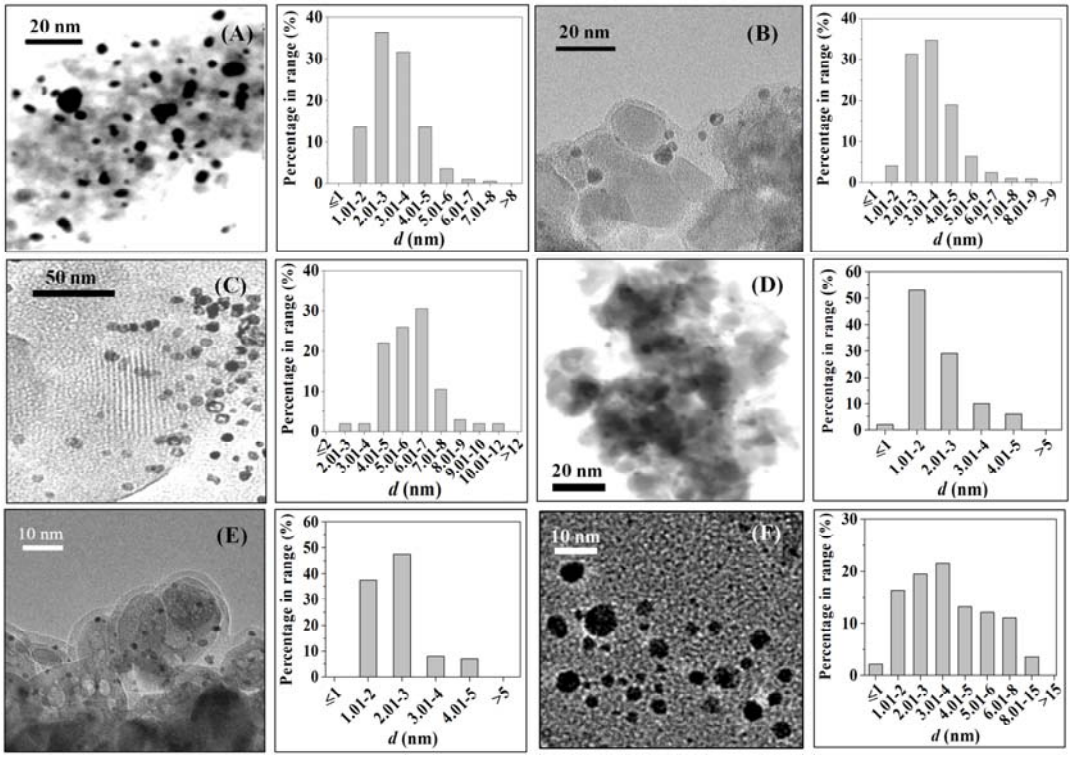
20 nm
(A)
Percentage in range (%)
d (nm)
20 nm
(B)
Percentage in range (%)
d (nm)
50 nm
(C)
Percentage in range (%)
d (nm)
(D)
20 nm
Percentage in range (%)
d (nm)
10 nm
(E)
Percentage in range (%)
d (nm)
10 nm
(F)
Percentage in range (%)
d (nm)

Fig. 5

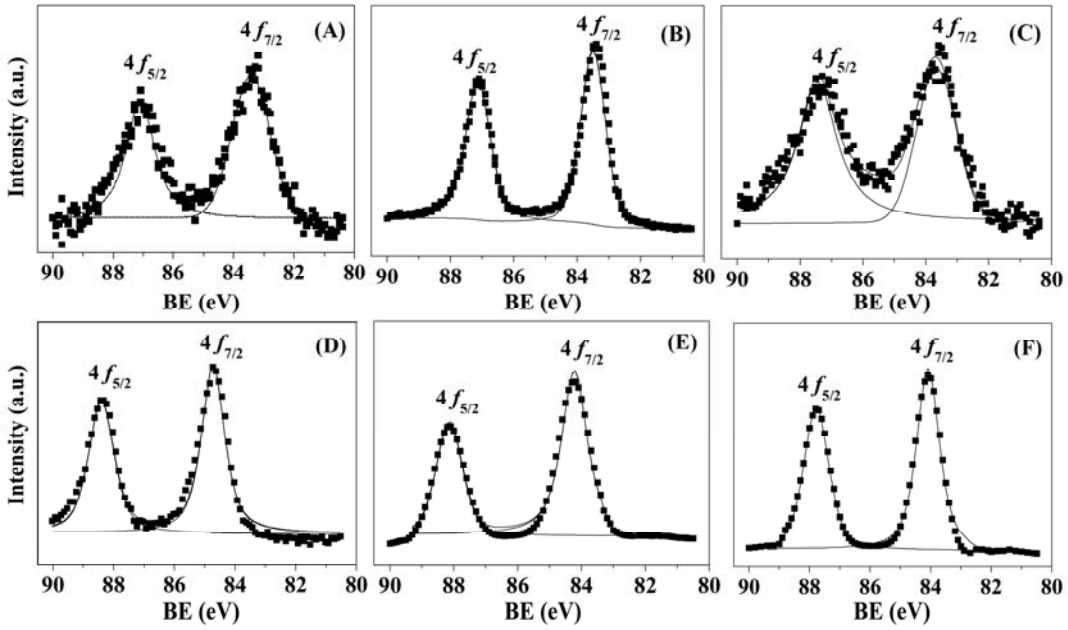

Fig. 6

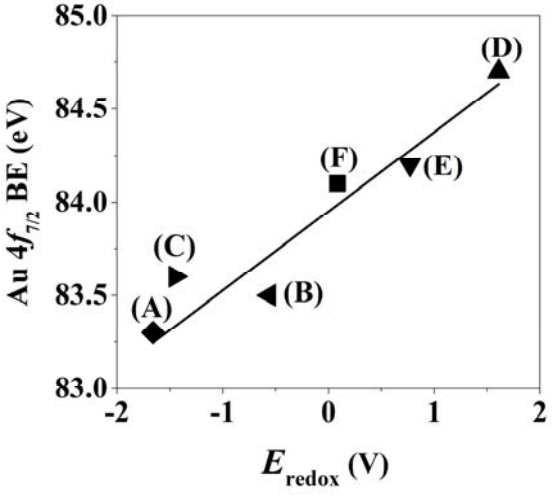

Fig. 7

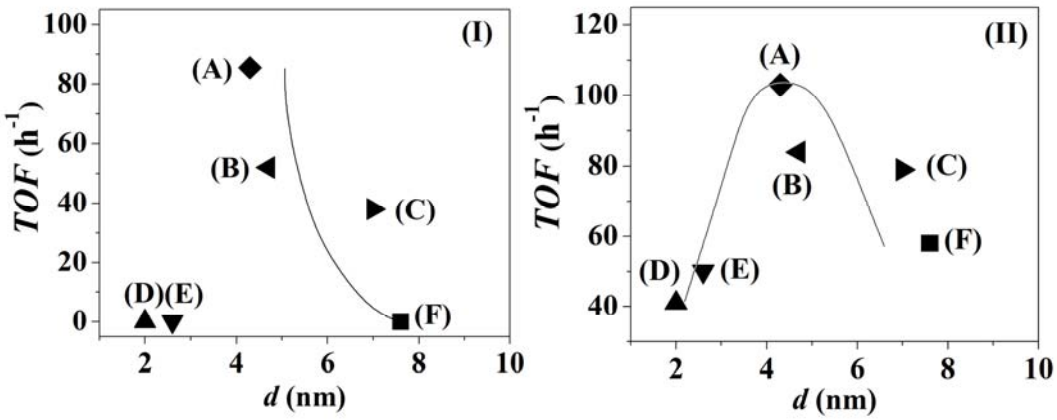

Fig. 8

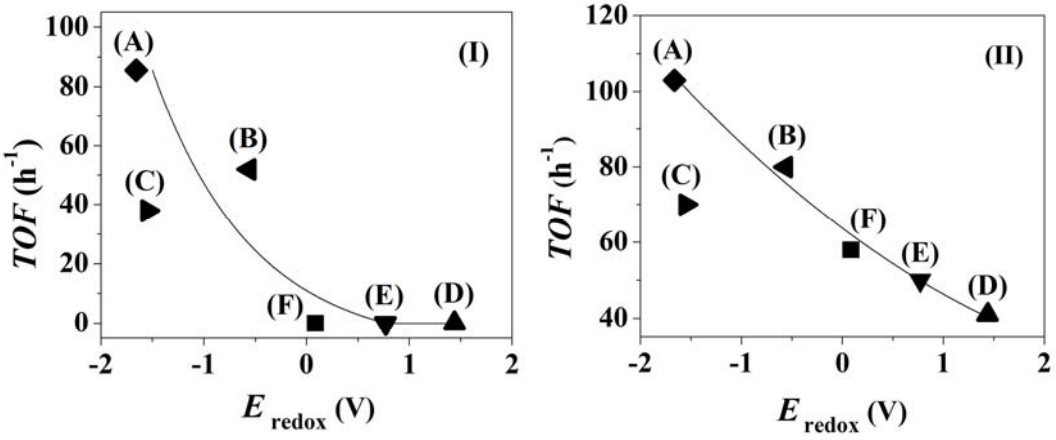

Fig. 9

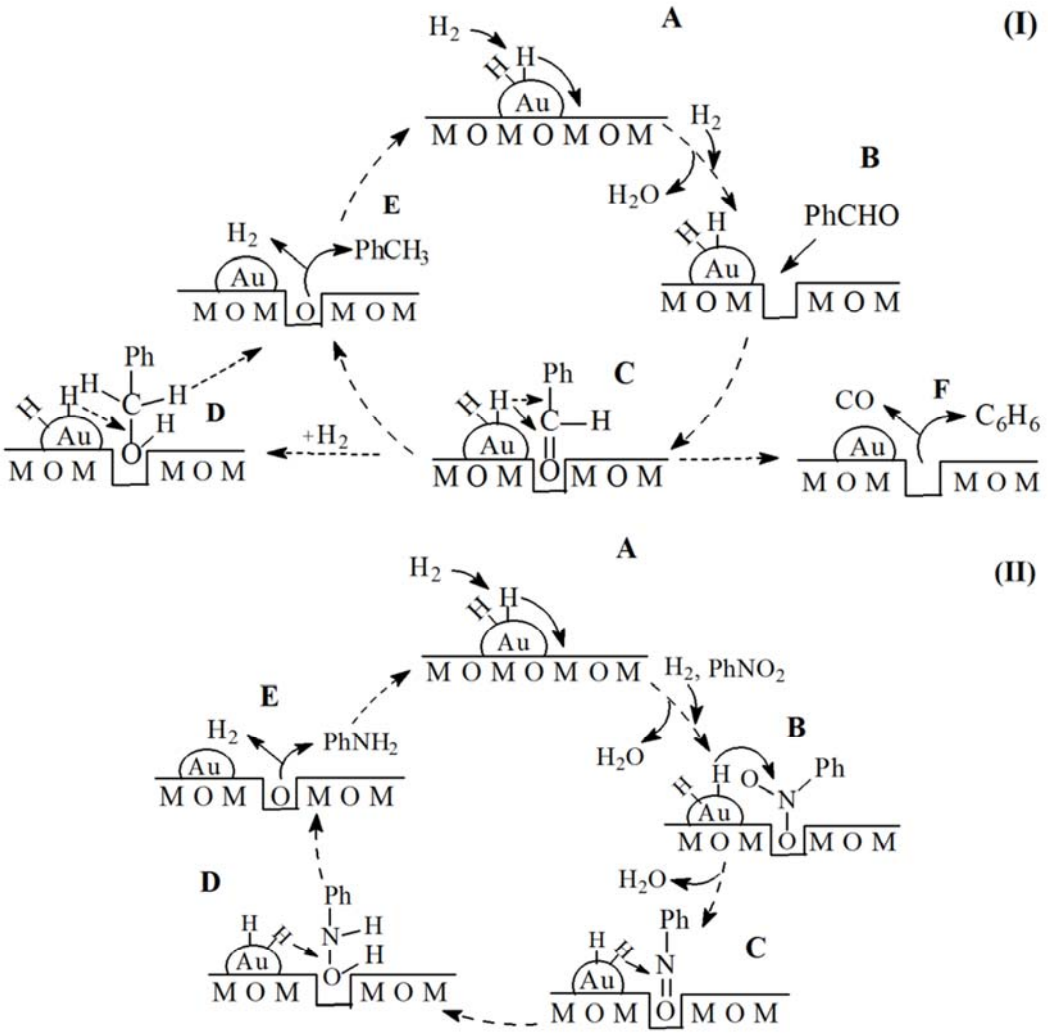

Fig. 10

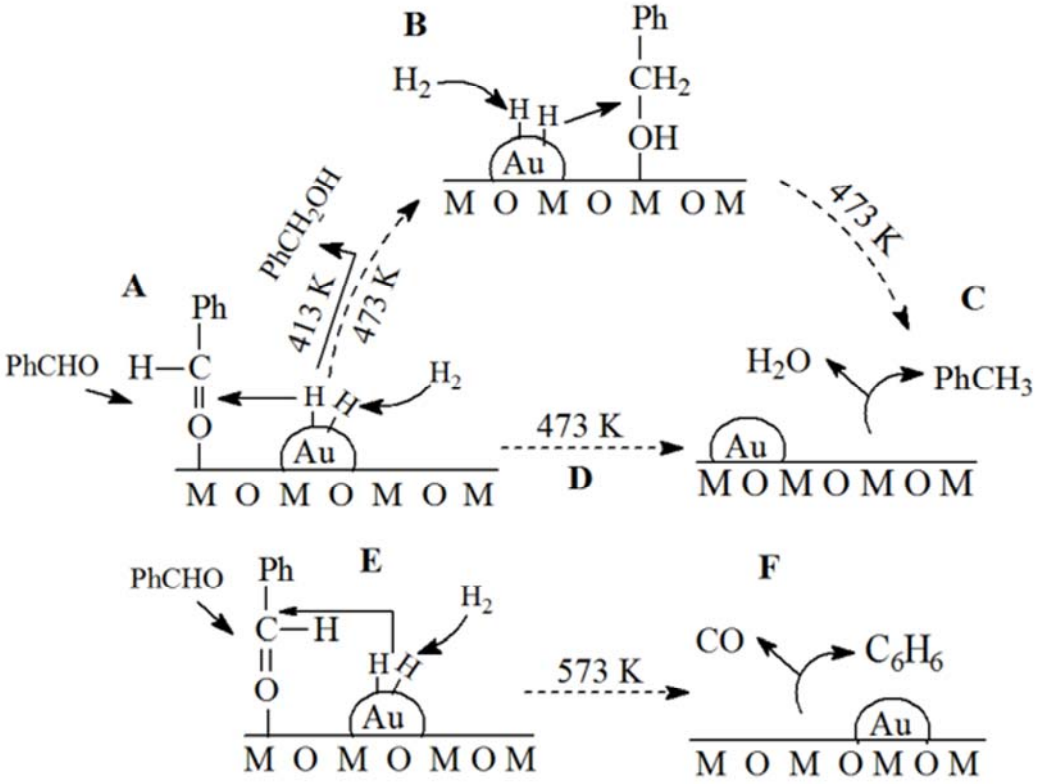
B
Ph
CH2
OH
H2
H H
Au
M O M O M O M
473 K
C
H2O
PhCH3
PhCH2OH
413 K
473 K
A
Ph
PhCHO
H—C
O
H
H
H2
Au
M O M O M O M
473 K
D
Au
M O M O M O M
PhCHO
E
Ph
C—H
O
H2
H H
Au
M O M O M O M
573 K
F
CO
C6H6
Au
M O M O M O M